MATERIALS SCIENCE

Vitality surveillance at distance using thin-film tandem-like narrowband near-infrared photodiodes with light-enhanced responsivity

Riccardo Ollearo[1], Xiao Ma[1], Hylke B. Akkerman[2], Marco Fattori[3], Matthew J. Dyson[1], Albert J. J. M. van Breemen[2], Stefan C. J. Meskers[1], Wijnand Dijkstra[1], René A. J. Janssen[1,4]*, Gerwin H. Gelinck[1,2]

Remote measurement of vital sign parameters like heartbeat and respiration rate represents a compelling challenge in monitoring an individual's health in a noninvasive way. This could be achieved by large field-of-view, easy-to-integrate unobtrusive sensors, such as large-area thin-film photodiodes. At long distances, however, discriminating weak light signals from background disturbance demands superior near-infrared (NIR) sensitivity and optical noise tolerance. Here, we report an inherently narrowband solution–processed, thin-film photodiode with ultrahigh and controllable NIR responsivity based on a tandem-like perovskite-organic architecture. The device has low dark currents ($<10^{-6}$ mA cm^{-2}), linear dynamic range >150 dB, and operational stability over time (>8 hours). With a narrowband quantum efficiency that can exceed 200% at 850 nm and intrinsic filtering of other wavelengths to limit optical noise, the device exhibits higher tolerance to background light than optically filtered silicon-based sensors. We demonstrate its potential in remote monitoring by measuring the heart rate and respiration rate from distances up to 130 cm in reflection.

INTRODUCTION

Unobtrusive, continuous monitoring of a patient's vitality is important in health diagnostics and would be facilitated by devices that can be used at the point of care. One of the most valuable and widely tracked vital signs is the heart rate, which can be measured, nowadays, noninvasively via electrocardiogram, ballistocardiography (1), photoplethysmography (PPG) (2), and thoracic motion tracking (3). Optical techniques, such as PPG and thoracic motion tracking, rely on the interaction of light with the human body and thus enable a remote, i.e., at distance, and entirely contactless assessment of the cardiorespiratory activity. This ensures more hygiene than on-skin devices and is highly desirable when monitoring newborns and people with skin conditions or when more comfort for the patient is required, such as during sleeping or resting time.

By sensing the volumetric variations of arterial blood in time as light oscillations, i.e., extracting a PPG signal, parameters such as heart rate, heart rate variability, and saturated blood oxygenation can be derived. This is carried out by illuminating subcutaneous tissues with a green, red, or near-infrared (NIR) light source followed by the detection of transmitted or back-reflected light with a photodetector. For remote monitoring, a NIR light source is preferred, as it is invisible and safer to the human eye (4), especially for prolonged exposure times of continuous monitoring but requires high NIR sensitivity from the photodetector. With increasing distances, challenges arise: Signals inevitably become weaker and have

lower integrity because of optical losses and uncontrolled fluctuations of ambient light, which raises the background noise. Resolving these complications is thereby an essential step toward the next generation of remote sensing devices. Commercial infrared cameras with advanced acquisition algorithms have been successfully used (5–7), but this approach relies on collecting light onto a small surface using expensive bulky optics that complicates their compactness and unobtrusive integration in everyday objects, such as bed mattresses, desk chairs, and seat cushions. In addition, camera-based remote PPG typically analyzes face images, which may imperil the individual's privacy (8). Here, solution-processed thin-film NIR photodetectors that can be processed cost effectively over large area on flexible, lightweight substrates have a clear advantage.

Solution-processed thin-film photodiodes (PDs) have seen tremendous progress in recent years. Several groups have investigated their use in direct-contact PPG (9–15). Organic PDs (OPDs) and, more recently, perovskite PDs (PPDs) have dominated the scene of this class of devices, bringing high photogeneration sensitivities, fast response times, and low noise levels (16–20). In addition, OPDs and PPDs exhibit tunable bandgaps, which can be controlled from the ultraviolet (UV) to the NIR via material composition and leveraged to vary the type (broad- and narrowband) of spectral sensitivity. For instance, NIR-sensitive PDs have been demonstrated by blending narrow-bandgap polymers in bulk heterojunctions (BHJs) (21–23) or by introducing tin (Sn) in lead halide perovskites (24–27). PDs with narrow or multiwavelength responsivity have been achieved without the use of optical filters, by using narrowband organic (28–31) and perovskite absorbers (32), by using the antibatic responsivity of thick active layers (33–36), or by constructing hybrid perovskite/organic hierarchical structures that self-filter parts of the visible spectrum (37–40).

[1]Molecular Materials and Nanosystems, Institute for Complex Molecular Systems, Eindhoven University of Technology, P.O. Box 513, 5600 MB Eindhoven, Netherlands. [2]TNO at Holst Centre, High Tech Campus 31, 5656 AE Eindhoven, Netherlands. [3]Integrated Circuits, Departments of Electrical Engineering, Eindhoven University of Technology, P.O. Box 513, 5600 MB Eindhoven, Netherlands. [4]Dutch Institute for Fundamental Energy Research, De Zaale 20, 5612 AJ Eindhoven, Netherlands.
*Corresponding author. Email: r.a.j.janssen@tue.nl

While these features hold great promise, discriminating weak NIR signals from ambient optical noise, i.e., high signal-to-(optical) noise ratio, is essential for remote monitoring. This implies that high photoresponsivity to vitality-relevant NIR wavelengths should be combined with a spectrally selective narrowband responsivity, thus eliminating a large part of the background light. Currently, however, filterless solution-processed narrowband PDs feature relatively low quantum conversion efficiencies, especially in the NIR region (33, 35, 37, 38, 41–44), and, to date, are still outperformed by optically filtered commercial Si. This restricts their use in several applications, including remote sensing.

Here, we report a self-filtering solution-processed PD having a narrowband and enhanced NIR responsivity that can be used to monitor heartbeat and respiration remotely. The PD is based on a perovskite-organic tandem-like architecture. It is obtained by stacking a narrow-bandgap BHJ film (PM6:Y6) directly on a wider-bandgap perovskite [FAMAPbI$_3$, with FA (formamidinium) and MA (methylammonium)] semiconductor with an electron-blocking film (poly{9,9-bis[3′-(N,N-dimethyl)-N-ethylammoinium-propyl-2,7-fluorene]-alt-2,7-(9,9-dioctylfluorene)}dibromide [PFN-Br]) as interlayer (structures of PM6, Y6, and PFN-Br are shown in fig. S1). Such a tandem-like architecture results in a narrowband spectral response with external quantum efficiency (EQE) peaking to 70% at 850 nm. When, however, exposed to additional green light, EQE values exceeding 200% are achieved. We show that such exceptional and adjustable NIR sensitivity facilitates the measurement of extremely weak light signals, thus enabling low-illumination vitality monitoring for reduced power consumptions. We then experimentally demonstrate remote heart rate and respiration detection from practical distances up to 130 cm. The PD also exhibits a higher filtering capability and, thus, lower susceptibility to optical noise than a broadband Si PD with optical filters. With this approach, a solution-processable device for remote heart rate and respiration monitoring is provided, paving the way to more dedicated and integrated vitality monitoring applications.

RESULTS

Tandem-like perovskite-organic PDs

The architecture and the working principle of the hybrid tandem-like PD are shown in Fig. 1. The device is based on two photoactive layers stacked on top of each other. Between these layers, we purposely deposited an optically inactive thin PFN-Br interlayer, the role of which will be discussed below. The active layers are made of a wider-bandgap perovskite layer combined with a narrow-bandgap organic BHJ consisting of a blend of donor and acceptor organic semiconductors, as schematically shown in Fig. 1A. All active layers are deposited by spin coating and sandwiched between a transparent front indium tin oxide/poly[bis(4-phenyl)(2,4,6-trimethylphenyl)amine] (ITO/PTAA) electrode and a reflective back electrode [C$_{60}$/bathocuproine (BCP)/Ag], resulting in a bottom-illuminated device. The device configuration resembles that of a tandem solar cell, albeit lacking a recombination junction, and will be referred to as tandem-like.

High-energy photons entering the diode via the transparent contact will be almost completely absorbed by the perovskite semiconductor, while low-energy photons are passed to the organic BHJ, where they can be absorbed depending on the BHJ bandgap (see Fig. 1B). By tuning the optical absorption edge of the two individual photoactive layers, it is possible to realize a narrowband NIR spectral response. This requires synergy between the photoactive layers and the PFN-Br interlayer, which plays a critical role in selectively blocking the collection of negatively charged photocarriers generated in the perovskite film. PFN-Br hinders the transport of electrons while facilitating the transport of holes (45). As a consequence, positive photocarriers generated in the BHJ layer are effectively collected at the electrodes, producing a photocurrent (Fig. 1C). A similar strategy has been reported before (39). The narrowband EQE spectrum is thus the effect of the photocurrent generated in the BHJ because of the longer wavelength absorption of the incident light. In first approximation and assuming unit internal quantum efficiency, the EQE spectrum of the tandem-like device corresponds to the difference between the EQE spectra of the OPD and PPD, i.e., max(EQE$_{OPD}$ − EQE$_{PPD}$, 0).

The location of the narrowband spectral window can be modified by material design. To demonstrate the versatility of this approach, we fabricated tandem-like PDs using mixed-halide Pb-based perovskite films with varied composition in combination with several organic donor-acceptor (D-A) combinations (Fig. 1D). Specifically, FA$_{0.66}$MA$_{0.34}$Pb(Br$_x$I$_{1-x}$)$_3$ was used as perovskite, with x = 0, 0.33, and 0.66, corresponding to bandgap energies (E_g) of approximately 1.56, 1.80, and 1.95 eV. For the BHJ layer, we used three donor polymers, i.e., poly[N-9'-heptadecanyl-2,7-carbazole-alt-5,5-(4',7'-di-2-thienyl-2',1',3'-benzothiadiazole)] (PCDTBT), PTB7-Th, and PM6, blended with four different acceptor materials, i.e., PC$_{61}$BM, Y6, IEICO4F, and COTIC4F, giving five different BHJs with bandgap edges ranging from 700 to 1200 nm. The chemical structures of the organic donor and acceptors are displayed in fig. S1. Single OPDs and PPDs were made for reference. The detailed description of the device fabrication is provided in Materials and Methods.

Figure 1D shows the EQE spectra of the five tandem-like PDs based on different perovskites and D-A BHJs. The measured narrowband EQE spectra of the tandem-like device (colored circles) can be constructed from the EQE spectra of the single-diode devices, i.e., max(EQE$_{OPD}$ − EQE$_{PPD}$, 0), which are plotted for comparison (black, red, and dashed lines). This series shows how both the spectral position and width of the narrowband peak can be easily controlled from the visible to the NIR (1200 nm) and tailored for the application of interest, without any additional optical filter. The low asymmetrical shoulder in the shorter λ region that is visible in some tandem-like devices is due to incomplete light filtering by the perovskite film. The transmitted light is absorbed in the BHJ, causing a small photocurrent at these wavelengths. Further variations may also arise from different light interference in the device (46).

Among them, we focus our attention on the FAMAPbI$_3$ − PM6:Y6 combination, as it displays a narrow EQE peak [full width at half maximum, <100 nm (47)] that is centered on 850 nm, which is a typical NIR wavelength used in PPG measurements. FAMAPbI$_3$ has been previously used in extremely sensitive PDs with ultralow dark currents (24). The PM6:Y6 blend has demonstrated excellent performance as non-fullerene active material in high-performance organic solar cells (48–50).

FAMAPbI$_3$ − PM6:Y6 PD characterization

The current density−voltage (J-V) characteristics recorded in the dark and under illumination for three different wavelengths, i.e.,
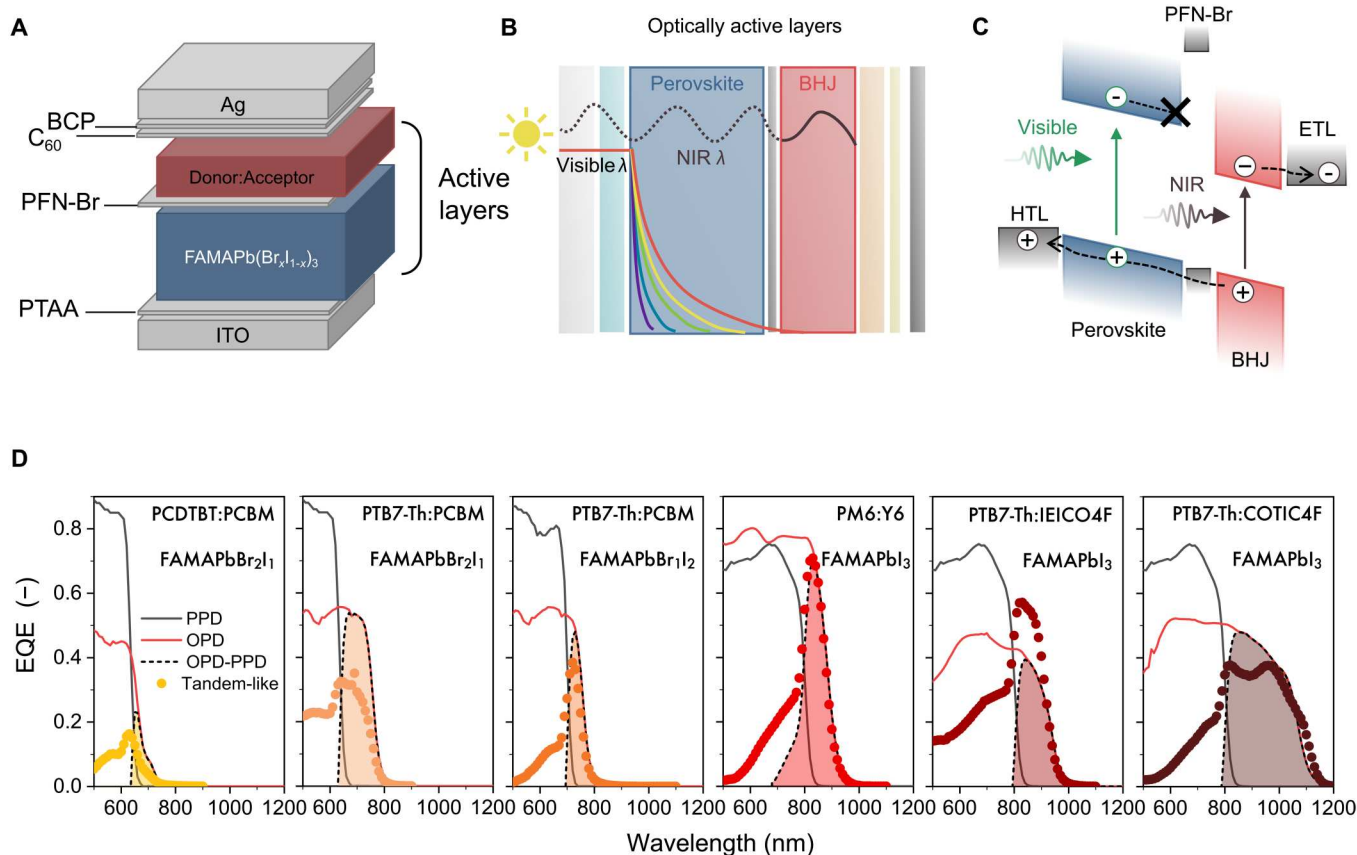
Fig. 1. Tandem-like device architecture, working principle, and materials. (**A**) Schematics of PD architecture. (**B**) Illustration of optical field distributions for visible and NIR wavelengths in the two optically active layers based on $FAMAPbI_3$ visible absorber and PM6:Y6 NIR absorber. For visible λ up to 650 nm, photons are predominantly absorbed by the perovskite film, while, for NIR λ (850 nm), photon absorption occurs within the organic BHJ layer and is subjected to cavity effects. (**C**) Schematics of the visible wavelengths filtering the tandem-like PD. HTL and ETL stand for hole and electron transport layer, respectively. The collection of photocarriers generated in the perovskite film is blocked by the perovskite/PFN-Br interface. (**D**) EQE as a function of wavelength (colored circle) of tandem-like devices using different perovskite/BHJ combinations, as indicated in the legend. EQE spectrum is compared with that of single PPD (black line) and single OPD (red line) and with the difference of their EQE shapes (dotted black line with colored area).

540, 660, and 850 nm, are shown in Fig. 2A. To exclude capacitive contributions (*24*), we determined the dark current density (J_D) in the range of −0.5 V to +0.3 V by measuring the current over time under constant applied voltages. We consider the latter measurement a more accurate way of determining J_D. The reverse J_D at $V = -0.5$ V is 2×10^{-7} mA cm^{-2}, and slowly decreases to 1×10^{-8} mA cm^{-2} when approaching $V = -0.1$ V. When illuminated with 0.5 mW cm^{-2} monochromatic 540-nm light, the photocurrent (J_{ph}) is low at $\sim 4 \times 10^{-3}$ mA cm^{-2}, while at 660 and 850 nm (and same light intensity), J_{ph} is 1.5×10^{-2} and 1×10^{-1} mA cm^{-2}, respectively, in agreement with the narrowband EQE profile. Notably, J_{ph} does not change much whether the device is reverse-biased (−0.5 V) or short-circuited (0 V). Considering the negligible bias dependence of the photocurrent, the device can be efficiently operated at $V = 0$ V.

At the PPG-relevant λ of 850 nm, the tandem-like PD exhibits a close to linear light intensity dependence of J_{ph} (at 0 V), with a fitted slope of $\alpha = 1.00$ (according to $J_{ph} \sim I^\alpha$) and a minimum detected light intensity of 1 nW cm^{-2}. This value is close to the minimum light intensity that our equipment can produce repeatedly and consistently at 850 nm. The recorded current noise spectral density (i_n)

of the device measured at 0 V is frequency independent ($f = 1$ to 100 Hz) and as low as 9×10^{-15} A Hz$^{-1/2}$ (fig. S3). At $V = -0.5$ V, i_n remains frequency-independent and increases slightly to $\sim 1 \times 10^{-14}$ A Hz$^{-1/2}$. By considering the measured resulting from noise as the lowest J_{ph}, the linear dynamic range (LDR), i.e., the span of light intensities within which the device output is linear to the incident light intensity, is >150 dB. At the highest end of light intensity range (1.5 mW cm^{-2}), no clear deviation from linearity is observed (Fig. 2B). The excellent linear response over a large NIR light intensity range is advantageous for measuring PPG remotely, as will be shown below.

The stability of the tandem-like PD over time was studied by illuminating the device for >8 hours with light pulses of $\lambda = 850$ nm and $f = 1$ Hz to mimic a real-life monitoring of a typical heartbeat at rest, i.e., 60 beats per minute (bpm), and of a duration corresponding to the recommended sleep time for a healthy adult (Fig. 2C) (*51*). No signs of degradation of the photoresponse were observed after the test period, indicating a promising operational stability and reliability to continuous tracking. With 5.6- and 6.05-μs rise and decay times (fig. S4), the device is sufficiently fast for accurately tracking the PPG waveform.
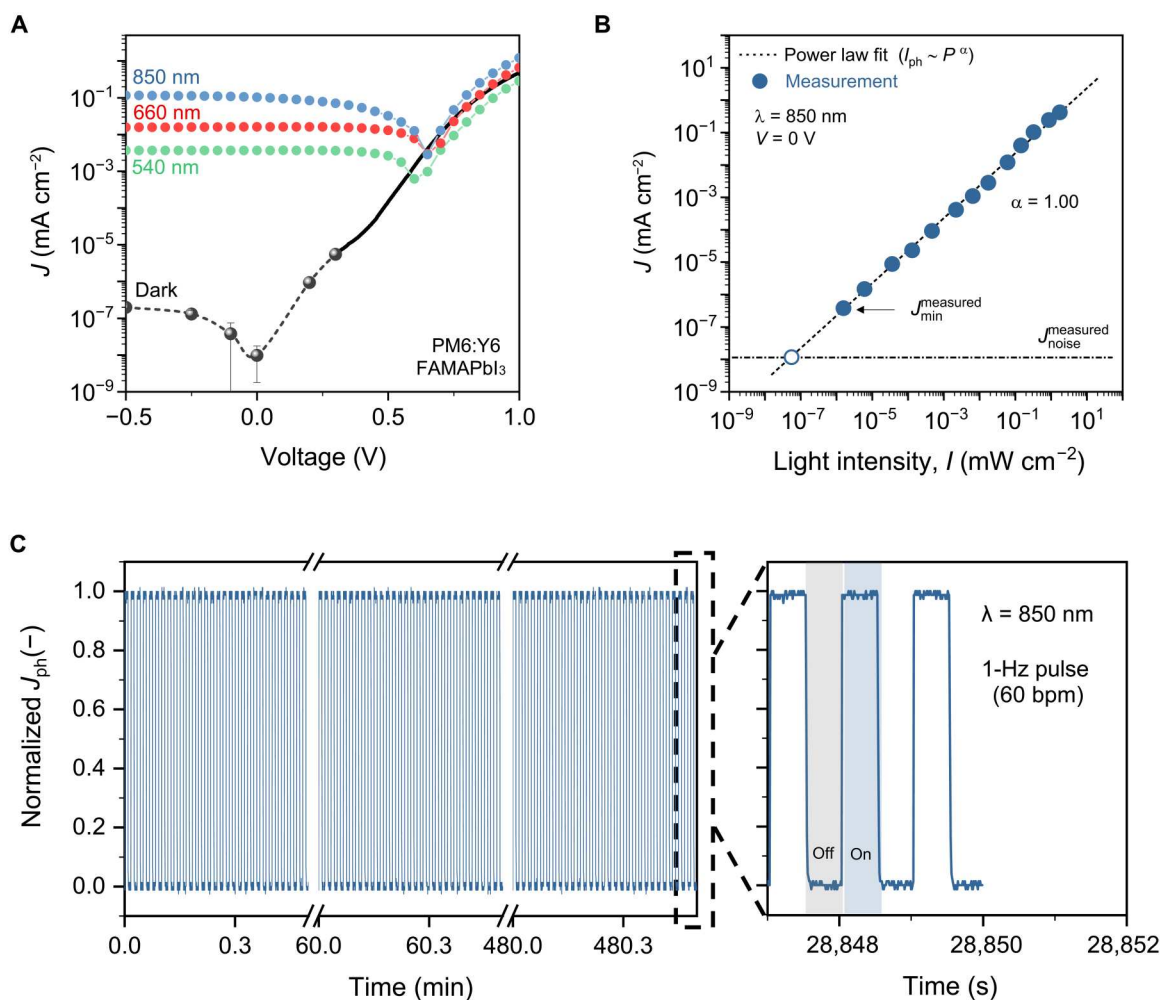
Fig. 2. Performance of narrowband PDs based on tandem-like architecture with FAMAPbI$_3$ and PM6:Y6 active layers. (**A**) J-V characteristics in the dark and under low light intensity illumination (0.5 mW cm^{-2}) for different wavelengths; in the dark, solid circles are current density values derived from constant voltage measurements over time at discrete biases (fig. S2). (**B**) Linearity plot measured at 0 V showing J_{ph} as a function of NIR light intensities (850 nm). (**C**) Continuous tracking over 8 hours of normalized transient photocurrent response of the device upon 850-nm light pulses of 1 Hz, corresponding to 60 bpm, a typical resting heartbeat.
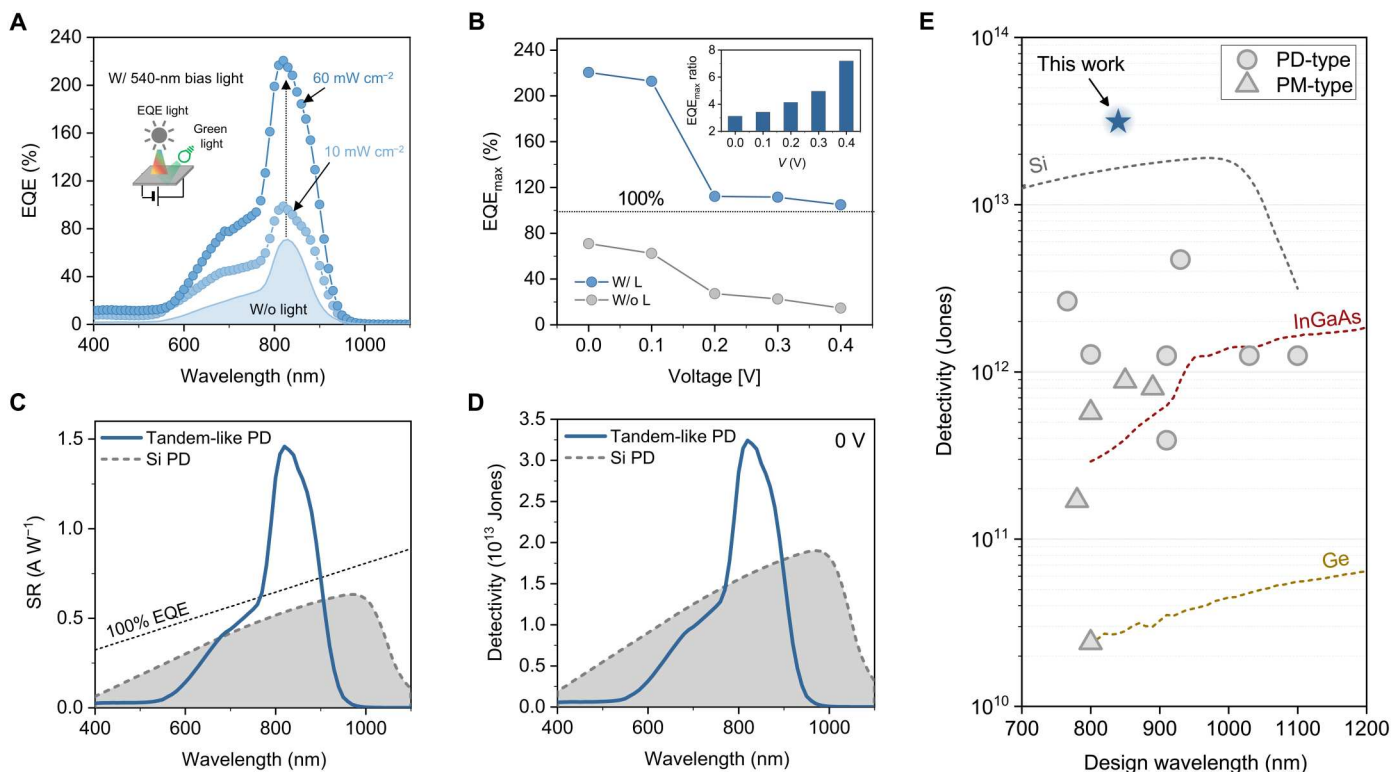
Enhanced NIR sensitivity by green light illumination

The FAMAPbI$_3$ − PM6:Y6 tandem-like PD showed a maximum EQE of 70% at 0 V (Fig 1C). At −1 V, the maximum of the EQE peak (EQE$_{max}$) increases to 80% (fig. S5), confirming the minor reverse bias dependence of the photoresponse. When the tandem-like PD is illuminated with an additional green light source (λ = 540 nm), as schematically represented in Fig. 3A, EQE$_{max}$ increases sharply. For a (green light) intensity of 10 mW cm^{-2}, EQE$_{max}$ is almost 100%, while for 60 mW cm^{-2}, it reaches 220%. This is exceptional for a PD characterized by low J_D and noise. Such light effect is also observed under a forward applied bias, where a reduction of the photoresponse, and thus of EQE, is expected (see Fig. 2A). For instance, at V = 0.4 V, the lower EQE$_{max}$ of 15% increases to 105%, as shown in Fig. 3B. This corresponds to a lower absolute EQE$_{max}$ value but higher relative enhancement (Fig. 3B, inset). Notably, the narrowband spectral response is retained, as shown in Fig. 3A (fig. S6).

We attribute this strong increase in EQE to above 100% to the transfer and collection of electrons photogenerated by the additional green light in the perovskite film to the BHJ and then to cathode because of a local energy barrier lowering at the PFN-Br interface. The event is triggered by the NIR-generated holes in the BHJ that are approaching the PFN-Br interface from the organic layer side. Therefore, the PFN-Br interlayer acts as an optoelectronic "valve" for electron extraction, and the incident NIR photons can open this valve in a way that resembles what occurs in a photomultiplication (52). The extent of this process varies as a function of the intensity of the additional green light, with which the NIR photoresponsivity of the device can therefore be regulated. A schematic illustration of the mechanism with a more detailed description is provided in fig. S7. As a control experiment, we fabricated a FAMAPbI$_3$ − PM6:Y6 PD without the PFN-Br interlayer. As shown in fig. S8, such a device shows neither the strong EQE enhancement nor the narrowband EQE profile, confirming the key role of the PFN-Br layer.

At its maximum enhancement, i.e., at V = 0 V and under 60 mW cm^{-2}, the narrowband spectral responsivity (SR) is ~1.5 A W^{-1} at 850 nm (Fig. 3C). At this wavelength, the tandem-like PD is almost

Fig. 3. Enhancement of NIR sensitivity by green light illumination. (**A**) EQE as function of wavelength measured with and without additional green (540 nm) light illumination, showing an enhancement in the NIR region. Green light intensities are indicated in the legend. (**B**) Corresponding EQE max (~830 nm) obtained with and without green illumination plotted as a function of applied bias voltage. For comparison, EQE_{max} under the additional 60 mW cm^{-2} 540-nm light is considered. The inset shows the relative enhancement of EQE due to the additional green light as a function of applied bias expressed as the ratio of EQE_{max} with and without green light. Data are extracted from EQE spectra (fig. S6). (**C**) Spectral responsivity (SR) of tandem-like PD (under 60 mW cm^{-2} 540-nm illumination) compared to that of commercial Si PD. Colored circles indicate the SR at 850 nm for our device, Si and ideal PDs having 100% EQE. (**D**) Detectivity at different wavelengths measured at 0 V for tandem-like PD under additional green light (blue solid line) and for commercial Si reference PD ($i_n = 1.2 \times 10^{-14}$ A Hz$^{-1/2}$) (gray dashed line). Graph in semilogarithmic scale is provided in fig. S10. (**E**) Comparison of noise current–based specific detectivity (D^*) of our device with state-of-the-art NIR narrowband solution–processed photodetectors (both PD and photomultiplication types, indicated in the legend as PD-type and PM-type, respectively) and with main commercial inorganic PDs, namely, Si (Thorlabs, FDS100-CAL), Ge (Thorlabs, FDG03-CAL), and InGaAs (Thorlabs, FGA21-CAL). The comparison focuses on reported devices with design wavelength lying in the NIR region between 700 and 1200 nm. Further details are provided in fig. S10.

three times more responsive than a commercial Si diode and two times more than an ideal PD with 100% EQE. Notably, such responsivity remains unaltered even 6 months after the fabrication of the device (fig. S9), indicating a long shelf-life. By calculating the specific detectivity from the measured noise current in dark condition using $D^* = SR\,(AB)^{1/2}\,i_n^{-1}$, with $A = 0.04$ cm^2 and $B = 1$ Hz, we achieved a peak D^* of ~3×10^{13} Jones at 850 nm (Fig. 3D), which surpasses that of inorganic Ge, InGaAs, and, notably, Si and is among the highest reported for NIR solution-processed PDs (53, 54). The device noise level under modulated green light remains largely unaltered (fig. S10). Our device excels, in particular, when compared with state-of-the-art narrowband photodetectors (both PD and photomultiplication types) with designed wavelength, i.e., peak of narrowband spectrum, in the NIR (Fig. 3E). Overall, the narrowband ultrahigh NIR sensitivity meets all requirements to ensure a high signal-to-(optical) noise ratio.

Enhanced NIR sensitivity for detection of extremely weak PPG signals

In a PPG measurement, high incident light intensities are generally preferred because of the severe light attenuation in the fingertip by skin structures (muscles, dermis, bones, tissues, and veins), often resulting in drops >90%, as we show in fig. S11. Considering that only a small portion (~1%) of the attenuated light contains information related to the cardiac activity, measuring PPG using weak (and low-powered) light sources can be prohibitive and lead to inconclusive readings. Enhancing the NIR sensitivity can help overcome this limitation. To show this, we performed low-illumination PPG measurements corresponding to light intensity variations lower than 1 nW cm^{-2}, which is close to the minimum detectable light intensity of the device (Fig. 2B).

In our experiment, we set the initial light intensity at 1.3 μW cm^{-2} so that only 0.8 nW cm^{-2} is modulated by heart-pumped blood flow and relevant for PPG. Additional optical losses occurred because of light-emitting diode (LED)–finger and finger-PD distances, shown schematically in Fig. 4A, where more experimental details are also provided. In particular, two measurements were
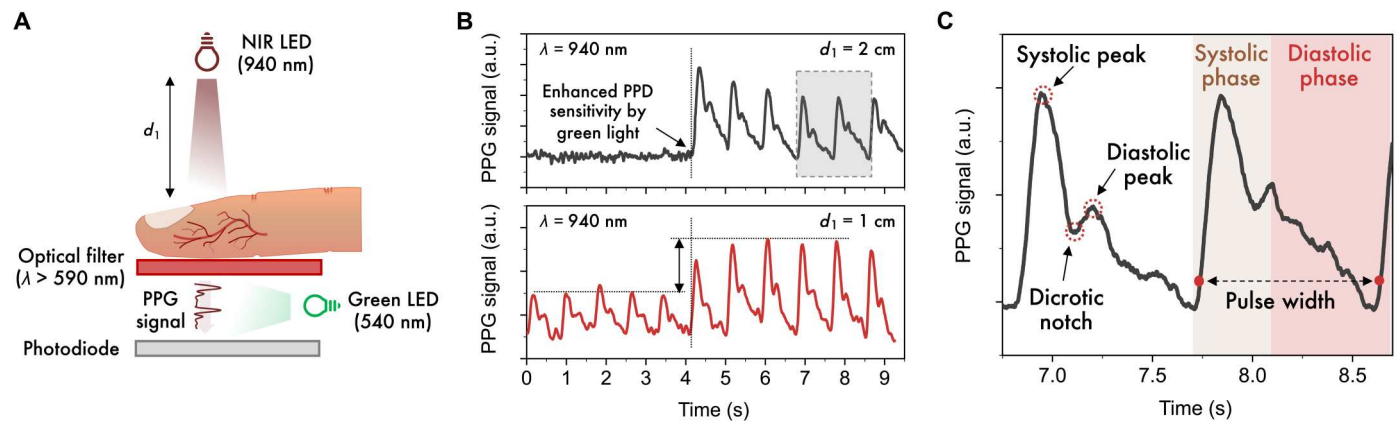
Fig. 4. Detecting weak PPG signals using the tandem-like PD with enhanced NIR sensitivity. (**A**) Schematic overview of the experimental conditions under which a PPG signal has been measured by the tandem-like PD with enhanced NIR sensitivity by green light illumination. As NIR light source, we used a LED emitting at 940 nm, i.e., at the edge of device SR, located at 1 or 2 cm above the finger. The PD was place instead ~1.5 cm below the finger, while the green LED (540 nm) was placed within this gap. In addition, an optical long-pass filter ($\lambda > 590$ nm) was placed underneath the finger to prevent unwanted PPG signal generation from the direct interaction of green light with the latter. (**B**) PPG signal measured in transmission from the finger as described in (A) without and with enhanced NIR sensitivity enabled by green light illumination. For the experiment, the green LED was driven at 1.5 V. (**C**) Enlargement of the PPG waveform indicated by the gray outline in (B), which shows the typical PPG waveform features, such as the systolic and diastolic peaks (and phases), dicrotic notch, and pulse width. a.u., arbitrary units.

performed, in which the distance between the LED and the finger was varied from 1 to 2 cm. The PPG setup was configured in such a way to intentionally undermine the already weak light before and after the interaction with the fingertip and obtain a weak or null PPG output signal.

Figure 4B shows the resulting PPG signals measured over time with our device at the two LED distances before and after the additional green illumination was turned on. In the absence of additional green light, i.e., in the first 4 s of the recording, the measured PPGs are relatively poor. In case of the larger LED-finger distance, no PPG signal was detectable at all. A similar result was obtained by using a commercial Si diode (fig. S12). When the green light is switched on and, thus, the sensitivity of the tandem-like PD increases, i.e., $t > 4$ s, full PPG waveforms could be recorded. The pulses measured by the tandem-like PD with enhanced NIR sensitivity show the systolic peak, dicrotic notch, and diastolic peak that typically characterize the rising (anacrotic) and descending (catacrotic) phases related to the variation of blood volume by cardiac dilation (Fig. 4C). From the systolic peak-to-peak interval, a heart rate of 67 bpm was extracted. Collectively, combining low-powered NIR and green LEDs resulted in a total power consumption of ~0.2 mW, which is two orders of magnitude lower than the power required by the single NIR LED (~40 mW) to produce a qualitatively similar PPG waveform. This effect is due to the enhanced responsivity under additional green light and the nonlinear power consumption of the NIR LED when increasing light intensity (figs. S11 and S13).
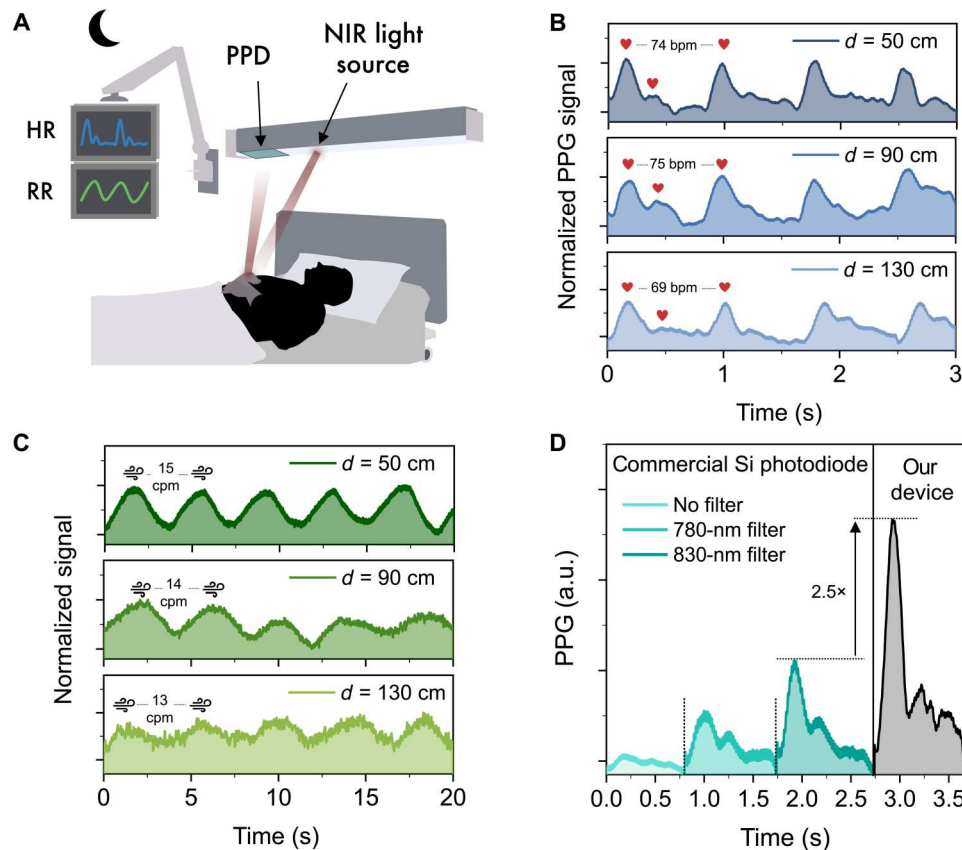
Remote vital sign measurements with tandem-like PD
Next, we used the tandem-like PD to measure both the heartbeat and respiration rate remotely. This would, for example, enable unobtrusive vital sign monitoring of a patient in a hospital bed during sleep with more comfort, as schematically proposed in Fig. 5A. To provide a proof of concept, we tracked both heart and respiration rates of a 29-year-old volunteer from three different distances by measuring the PPG signal (for heart rate) and the thoracic

motion (for respiration rate) from the individual's hand and chest, respectively. Both the device and the NIR light source were located at 50, 90, and 130 cm from the body locations, as schematically shown in fig. S14A. A photograph of the experimental setup for heartbeat monitoring is shown in fig. S14B. As NIR light source, we used a LED emitting at 850 nm that matches the responsivity peak of our device. The lower risk and disturbance to the human eye of NIR radiation then allowed us to drive the LED at higher voltage (8 V) for a brighter light intensity to compensate for the longer distances. The precise intensity value interacting with the body parts was, however, hard to estimate because of the wide diffusion angle (35°) of the light beam of the LED and the undefined illuminated area of the body. The measurements were performed indoor during a sunny day with the curtains partially closed to replicate the ambient illumination of a room during a typical daytime sleeping (fig. S14B).

Figure 5B shows the normalized PPG signals measured by the tandem-like PD at the three distances mentioned above, i.e., 50, 90, and 130 cm. At each distance, the systolic and diastolic phases are observed, from which heart rates of 74, 75, and 69 bpm were extracted, respectively. In Fig. 5C, the respiration rates measured at the same distances are shown, resulting in 15, 14, and 13 cpm (cycles per minute), which well lie in the respiratory rate range of a healthy adult at rest (55). The variation of reflected light intensity due to respiratory thoracic motion was estimated through clothing. Both measured signals by the device were amplified by a preamplifier and normalized for comparison. More details on the acquisition technique are provided in Materials and Methods.

Notably, no accurate alignment between the LED and the PD was needed to detect the PPG signal at each distance. A rough directing of the LED light and the PD toward the interested acquisition area of the body was sufficient to read both heart and respiration rates. This would impose fewer constraints to future device integration into the individual's surroundings, enabling multipoints monitoring and better coverage. In addition, several PDs could be fabricated in parallel so that the failure of a single PD

Fig. 5. Demonstration of vital sign measurements at distance for constant, wireless monitoring. (**A**) Schematic illustration of the application of the tandem-like PD in a hospital bed for heart and respiration rate monitoring at distance of a patient during sleep/resting time. The optical noninvasive wireless setup that can be integrated in the hospital's equipment and maximize the comfort of the patient. (**B**) Normalized PPG signal measured at different PD-finger distances using NIR light (850 nm). (**C**) Normalized respiration rate signal measured through clothing at different PD-chest distances using NIR light (850 nm). (**D**) Comparison of PPG signals measured at distance (d = 50 cm) under the same experimental conditions using our tandem-like device and a broadband commercial Si PD without and with 780- and 830-nm optical filters to suppress ambient optical noise.

would not lead to a failing PPG signal. For completeness, heart rate was also measured in transmissive mode, with the LED located in proximity of the fingertip and in opposite position compared to the PD. In this case, PPG signals were acquired at longer PD-hand distances of 100, 150, and 210 cm (fig. S15).

Last, we compared the optical noise tolerance during remote PPG measurements with that of a broadband commercial Si PD (Thorlabs, FDS100-CAL) equipped with optical filters. Measurements were performed under the same conditions for each device (d = 50 cm, reflective mode, same applied voltage to the LED as above). When no optical filter is used, the broadband Si diode hardly discriminates the PPG waveform. Stronger PPG signals are discerned when optical cutoff filters are used, as shown in Fig. 5D. The largest PPG signal (obtained with 830-nm filter) is, however, 2.5× lower than that recorded with our device, proving the higher filtering efficacy of our narrowband device. As a result, PPG measurement at longer distances has not been possible with an optically filtered Si diode.

DISCUSSION

We have developed a self-filtering solution-processed, thin-film PD with enhanced NIR responsivity for heartbeat and respiration monitoring at distance using a tandem-like structure made of perovskite-organic BHJ active layers and a PFN-Br interlayer. Within this architecture, the stacking of the two active layers simplifies the device integration and enables a filterless narrowband spectral response, which can be tuned from visible to NIR by selecting the appropriate combination of perovskite and organic semiconductor materials. By integrating the composition of interest (FAMAPbI$_3$ – PM6:Y6) into a PD, we achieved low dark and noise current, a wide LDR > 150 dB under NIR light (850 nm), and a stable device response over time (>8 hours) to pulsed light. We have demonstrated an enhancement of the device sensitivity to NIR (850 nm) upon additional green light illumination, expressed in terms of EQE values exceeding 200%, SR of 1.5 A W^{-1}, and D^* of 3×10^{13} Jones. This exceptional performance allowed us to detect extremely weak PPG signals resulting from low illumination source. We have also demonstrated remote heart rate and respiration rate monitoring from beyond 130 cm, which shapes a noninvasive, more comfortable monitoring scenario. In addition, in comparison with an optically filtered broadband Si PD, our device exhibits a higher filtering

capability and, thus, lower susceptibility to optical ambient noise. These features, coupled with a cost-effective large-area processing, make this tandem-like PD promising for the next generation of contactless vital sign monitoring devices.

MATERIALS AND METHODS

Materials
All materials were purchased from commercial sources and used without further purification unless otherwise mentioned. PbI_2 and $PbBr_2$ (99.99%) were purchased from TCI Chemicals. All the organic salts for perovskites were purchased from GreatCell Solar. All the solvents were bought from Sigma-Aldrich. PCDTBT, PTB7-Th, IEICO-4F, COTIC-4F, and $PC_{61}BM$ were purchased from 1-Material Inc., while PM6, Y6, and PFN-Br were purchased from Solarmer Materials Inc.

Active layer deposition
Solution preparation and film deposition were performed in an N_2-filled glove box. $FA_{0.66}MA_{0.34}Pb(Br_xI_{1-x})_3$ was prepared via two-step spin coating according to a previous publication from our group (56). For the molar fraction (x) of 0 and 0.33, 553.2 mg of PbI_2 was dissolved in N,N'-dimethylformamide (DMF; 0.876 ml) and dimethyl sulfoxide (DMSO; 0.0864 ml), while for $x = 0.66$, 276.6 mg of PbI_2 and 220.2 mg of $PbBr_2$ were dissolved in the same amount of DMF and DMSO. The solutions were spin-coated at 3000 rpm for 30 s. Then, the organic solutions made of 53.48 mg of FAI and 25.6 mg of MAI (for $x = 0$), 39.23 mg of FABr, and 17.57 mg of MABr (for $x = 0.33$ and 0.66) in isopropanol (1 ml) were spin-coated at 3000 rpm for 60 s. The perovskite films were thermally annealed at 100°C for 30 min. The PFN-Br interlayer was prepared by dissolving PFN-Br in methanol (0.5 mg ml^{-1}) and by spin coating the solution at 3000 rpm for 30 s, followed by a thermal anneal at 90°C for 5 min. PCDTBT:$PC_{61}BM$ film was prepared by blending PCDTBT with $PC_{61}BM$ (1:4 w/w) in chlorobenzene (CB) (35 mg ml^{-1}) and by spin coating the solution at 3000 rpm for 30 s, followed by a thermal anneal at 60°C for 15 min. PTB7-Th:$PC_{61}BM$ film was prepared by blending PTB7-Th with $PC_{61}BM$ (1:1.5 w/w) in CB (20 mg ml^{-1}) and by spin coating the solution at 3000 rpm for 30 s, followed by a thermal anneal at 90°C for 15 min. PTB7-Th:IEICO-4F and PTB7-Th:COTIC-4F films were prepared by blending PTB7-Th with IEICO-4F (1:1.5 w/w) and COTIC-4F (1:1.5 w/w), respectively, in CB (20 mg ml^{-1}) and by spin coating the solutions at 3000 rpm for 30 s, followed by a thermal anneal at 90°C for 15 min. PM6:Y6 film was prepared by blending PM6 with Y6 (1:1.2 w/w) in chloroform (16 mg ml^{-1}) and by spin coating the solution at 3000 rpm for 30 s, followed by a thermal anneal at 110°C for 10 min.

PD fabrication
All tandem-like PDs and single PPDs share the same device stack, which was fabricated as follows. Transparent ITO (135 nm) was deposited by sputtering on glass and patterned via photolithography to shape the bottom electrode. On top, a thin SiN (50 nm) layer was deposited and structured via dry etch to define the active area of the ITO electrodes and to prevent leakage currents (57, 58). Next, a 30-min UV-ozone treatment was performed on the substrates, followed by PTAA (3 mg ml^{-1} in toluene) deposition via spin coating at 5700 rpm for 30 s. The layer was then thermally annealed at 100°C for 10

min. C_{60} (20 nm; SES Research), BCP (8 nm; Lumtec), and the Ag top electrode (100 nm) were thermally evaporated under high vacuum ($\approx 10^{-7}$ mbar).

Single OPDs were fabricated using a different stack. An ITO film (100 nm) was sputtered on glass first, followed by an amorphous indium gallium zinc oxide (IGZO) film (16 nm) deposited via sputtering at room temperature with a metal ratio of 1:1:1. Both the ITO and IGZO were then structured by photolithography. On top, an SU-8 layer was deposited and patterned to cover the perimeter of the electrodes. After the deposition of the active films, 15 nm of MoO_3 and 100 nm of Ag were thermally evaporated as top contact under high vacuum ($\approx 10^{-7}$ mbar).

Tandem-like PD characterization
Dark current density was measured in an N_2-filled glove box through manual probes connected to an Agilent 4155C semiconductor parameter analyzer. For an accurate determination of J_D, a constant reverse voltage bias was applied over time to eliminate unwanted charging effects. The stability of the device to light pulses over time was measured using a digital oscilloscope (Tektronix, TDS3032B) and NIR light pulses (850 nm) generated by a LED driven by a wave function generator (PeakTech, 4040). Within the same setup, the photocurrent response of the PPD to different light intensity was measured using the same NIR LED, which was calibrated with a reference silicon PD (Thorlabs, FDS100-CAL). The EQE custom-made setup consisted of a tungsten-halogen lamp, a monochromator (Oriel, Cornerstone 130), a chopper, a preamplifier (Stanford Research Systems, SR570), and a lock-in amplifier (Stanford Research Systems, SR830 DSP). All EQE measurements were performed using a lock-in detection and modulated probe light to extract the photocurrent at the modulation frequency and reject all other frequency and continuous components. The devices were transferred in the setup through a N_2-filled box equipped with a quartz window, on which a circular aperture (diameter, 1 mm) was applied. The additional green light illumination was provided by shining a 530-nm LED toward the device following the same optical path of the EQE light. EQE signal was calibrated with a reference silicon solar cell. The SD of this setup is less than 0.005 electron per photon (in the range 350 to 1050 nm of wavelengths). Noise measurements were performed in a battery-powered current-to-voltage conversion readout circuit developed with off-the-shelf components. The setup is arranged in a metal enclosure to shield the device from electromagnetic interference and keep it in dark conditions. The PD (active area of 4 mm^2) was connected by means of two probes and triaxial cables to a trans-impedance amplifier (TIA) implemented with the operation amplifier Analog Devices (ADA4530). The device was biased by applying an adjustable DC voltage source to the noninverting terminal of the TIA. The output of the TIA is fed to an active band-pass amplifier (built using Analog Devices AD8065 operational amplifier) and lastly read out by a dynamic signal analyzer (HP35670A).

Heartbeat and respiration rate measurement setup
Measurements were performed by connecting, in sequence, the PD by means of small probes (integrated in a custom-made three-dimensional printed holder) to a signal amplifier (Stanford Research Systems, SR570), a lock-in amplifier (Stanford Research Systems, SR830 DSP), and an oscilloscope (Tektronix, TDS3032B). Measurements were carried out in ambient conditions, for which a

protective barrier was laminated onto the PD. As light sources, two NIR LEDs (940 and 850 nm) and a green LED (540 nm) were powered by a wave function generator (PeakTech, 4040). During the acquisition, raw signals have been electronically filtered using a band-pass digital filter from 0.5 to 10 Hz to remove the out-of-band and non-pulsatile (DC) components. In case of respiration rate monitoring, the signal amplifier (Stanford Research Systems, SR570) was directly connected to the oscilloscope (Tektronix, TDS3032B), without using the lock-in amplifier. In addition, a band-pass digital filter from 0.1 to 10 Hz was used.

Supplementary Materials
This PDF file includes:
Figs. S1 to S15
Table S1
Legend for data S1
References

Other Supplementary Material for this manuscript includes the following:
Data S1

REFERENCES AND NOTES

1. O. T. Inan, P.-F. Migeotte, K.-S. Park, M. Etemadi, K. Tavakolian, R. Casanella, J. Zanetti, J. Tank, I. Funtova, G. K. Prisk, M. Di Rienzo, Ballistocardiography and seismocardiography: A review of recent advances. *IEEE J. Biomed. Health Inform.* **19**, 1414–1427 (2015).

2. J. Park, H. S. Seok, S.-S. Kim, H. Shin, Photoplethysmogram analysis and applications: An integrative review. *Front. Physiol.* **12**, 808451 (2022).

3. T. Allsop, G. Lloyd, R. S. Bhamber, L. Hadzievski, M. Halliday, D. J. Webb, I. Bennion, Cardiac-induced localized thoracic motion detected by a fiber optic sensing scheme. *J. Biomed. Opt.* **19**, 117006 (2014).

4. F. C. Delori, R. H. Webb, D. H. Sliney; American National Standards Institute, Maximum permissible exposures for ocular safety (ANSI 2000), with emphasis on ophthalmic devices. *J. Opt. Soc. Am. A. Opt. Image Sci. Vis.* **24**, 1250–1265 (2007).

5. Q. Zhang, Y. Zhou, S. Song, G. Liang, H. Ni, Heart rate extraction based on near-infrared camera: Towards driver state monitoring. *IEEE Access* **6**, 33076–33087 (2018).

6. E. M. Nowara, T. K. Marks, H. Mansour, A. Veeraraghavan, Near-infrared imaging photoplethysmography during driving. *IEEE Trans. Intell. Transp. Syst.* **23**, 3589–3600 (2022).

7. N. Martinez, M. Bertran, G. Sapiro, H. Wu, Non-contact photoplethysmogram and instantaneous heart rate estimation from infrared face video, in *2019 IEEE International Conference on Image Processing* (IEEE, 2020).

8. W. Wang, A. C. Den Brinker, G. De Haan, Single-element remote-PPG. *I.E.E.E. Trans. Biomed. Eng.* **66**, 2032–2043 (2019).

9. N. Cui, Y. Song, C. H. Tan, K. Zhang, X. Yang, S. Dong, B. Xie, F. Huang, Stretchable transparent electrodes for conformable wearable organic photovoltaic devices. *npj Flex. Electron.* **5**, 31 (2021).

10. Y. Khan, D. Han, A. Pierre, J. Ting, X. Wang, C. M. Lochner, G. Bovo, N. Yaacobi-Gross, C. Newsome, R. Wilson, A. C. Arias, A flexible organic reflectance oximeter array. *Proc. Natl. Acad. Sci. U.S.A.* **115**, E11015–E11024 (2018).

11. C. M. Lochner, Y. Khan, A. Pierre, A. C. Arias, All-organic optoelectronic sensor for pulse oximetry. *Nat. Commun.* **5**, 5745 (2014).

12. C. Fuentes-Hernandez, W. F. Chou, T. M. Khan, L. Diniz, J. Lukens, F. A. Larrain, V. A. Rodriguez-Toro, B. Kippelen, Large-area low-noise flexible organic photodiodes for detecting faint visible light. *Science* **370**, 698–701 (2020).

13. G. Simone, D. Tordera, E. Delvitto, B. Peeters, A. J. J. M. van Breemen, S. C. J. Meskers, R. A. J. Janssen, G. H. Gelinck, High-accuracy photoplethysmography array using near-infrared organic photodiodes with ultralow dark current. *Adv. Opt. Mater.* **8**, 1901989 (2020).

14. Z. Wu, W. Yao, A. E. London, J. D. Azoulay, T. N. Ng, Temperature-dependent detectivity of near-infrared organic bulk heterojunction photodiodes. *ACS Appl. Mater. Interfaces* **9**, 1654–1660 (2017).

15. J. Simões, T. Dong, Z. Yang, Non-fullerene acceptor organic photodetector for skin-conformable photoplethysmography applications. *Adv. Mater. Interfaces* **9**, 2101897 (2022).

16. B. R. Sutherland, A. K. Johnston, A. H. Ip, J. Xu, V. Adinolfi, P. Kanjanaboos, E. H. Sargent, Sensitive, fast, and stable perovskite photodetectors exploiting interface engineering. *ACS Photonics* **2**, 1117–1123 (2015).

17. B. Yang, F. Zhang, J. Chen, S. Yang, X. Xia, T. Pullerits, W. Deng, K. Han, Ultrasensitive and fast all-inorganic perovskite-based photodetector via fast carrier diffusion. *Adv. Mater.* **29**, 1703758 (2017).

18. V. Adinolfi, O. Ouellette, M. I. Saidaminov, G. Walters, A. L. Abdelhady, O. M. Bakr, E. H. Sargent, Fast and sensitive solution-processed visible-blind perovskite UV photodetectors. *Adv. Mater.* **28**, 7264–7268 (2016).

19. F. Guo, Z. Xiao, J. Huang, Fullerene photodetectors with a linear dynamic range of 90 dB enabled by a cross-linkable buffer layer. *Adv. Opt. Mater.* **1**, 289–294 (2013).

20. J. Liu, J. Jiang, S. Wang, T. Li, X. Jing, Y. Liu, Y. Wang, H. Wen, M. Yao, X. Zhan, L. Shen, Fast response organic tandem photodetector for visible and near-infrared digital optical communications. *Small* **17**, 2101316 (2021).

21. J. Lee, S. J. Ko, H. Lee, J. Huang, Z. Zhu, M. Seifrid, J. Vollbrecht, V. V. Brus, A. Karki, H. Wang, K. Cho, T. Q. Nguyen, G. C. Bazan, Side-chain engineering of nonfullerene acceptors for near-infrared organic photodetectors and photovoltaics. *ACS Energy Lett.* **4**, 1401–1409 (2019).

22. C. Xu, P. Liu, C. Feng, Z. He, Y. Cao, Organic photodetectors with high detectivity for broadband detection covering UV-vis-NIR. *J. Mater. Chem. C* **10**, 5787–5796 (2022).

23. W. Yang, W. Qiu, E. Georgitzikis, E. Simoen, J. Serron, J. Lee, I. Lieberman, D. Cheyns, P. Malinowski, J. Genoe, H. Chen, P. Heremans, Mitigating dark current for high-performance near-infrared organic photodiodes via charge blocking and defect passivation. *ACS Appl. Mater. Interfaces* **13**, 16766–16774 (2021).

24. R. Ollearo, J. Wang, M. J. Dyson, C. H. L. Weijtens, M. Fattori, B. T. Van Gorkom, A. J. J. M. Van Breemen, S. C. J. Meskers, R. A. J. Janssen, G. H. Gelinck, Ultralow dark current in near-infrared perovskite photodiodes by reducing charge injection and interfacial charge generation. *Nat. Commun.* **12**, 7277 (2021).

25. A. Moeini, L. Martínez-Sarti, K. P. S. Zanoni, M. Sessolo, D. Tordera, H. J. Bolink, Semitransparent near-infrared Sn–Pb hybrid perovskite photodetectors. *J. Mater. Chem. C* **10**, 13878–13885 (2022).

26. X. Xu, C. C. Chueh, P. Jing, Z. Yang, X. Shi, T. Zhao, L. Y. Lin, A. K. Y. Jen, High-performance near-IR photodetector using low-bandgap $MA_{0.5}FA_{0.5}Pb_{0.5}Sn_{0.5}I_3$ perovskite. *Adv. Funct. Mater.* **27**, 1701053 (2017).

27. W. Wang, D. Zhao, F. Zhang, L. Li, M. Du, C. Wang, Y. Yu, Q. Huang, M. Zhang, L. Li, J. Miao, Z. Lou, G. Shen, Y. Fang, Y. Yan, Highly sensitive low-bandgap perovskite photodetectors with response from ultraviolet to the near-infrared region. *Adv. Funct. Mater.* **27**, 1703953 (2017).

28. S. J. Lim, D. S. Leem, K. B. Park, K. S. Kim, S. Sul, K. Na, G. H. Lee, C. J. Heo, K. H. Lee, X. Bulliard, R. I. Satoh, T. Yagi, T. Ro, D. Im, J. Jung, M. Lee, T. Y. Lee, M. G. Han, Y. W. Jin, S. Lee, Organic-on-silicon complementary metal-oxide-semiconductor colour image sensors. *Sci. Rep.* **5**, 7708 (2015).

29. K. H. Lee, G. H. Lee, D. S. Leem, J. Lee, J. W. Chung, X. Bulliard, H. Choi, K. B. Park, K. S. Kim, Y. W. Jin, S. Lee, S. Y. Park, Dynamic characterization of green-sensitive organic photodetectors using nonfullerene small molecules: Frequency response based on the molecular structure. *J. Phys. Chem. C* **118**, 13424–13431 (2014).

30. D. M. Lyons, A. Armin, M. Stolterfoht, R. C. R. Nagiri, R. D. Jansen-Van Vuuren, B. N. Pal, P. L. Burn, S. C. Lo, P. Meredith, Narrow band green organic photodiodes for imaging. *Org. Electron.* **15**, 2903–2911 (2014).

31. L. Gao, C. Ge, W. Li, C. Jia, K. Zeng, W. Pan, H. Wu, Y. Zhao, Y. He, J. He, Z. Zhao, G. Niu, X. Guo, F. P. G. de Arquer, E. H. Sargent, J. Tang, Flexible filter-free narrowband photodetector with high gain and customized responsive spectrum. *Adv. Funct. Mater.* **27**, 1702360 (2017).

32. J. Li, J. Wang, J. Ma, H. Shen, L. Li, X. Duan, D. Li, Self-trapped state enabled filterless narrowband photodetections in 2D layered perovskite single crystals. *Nat. Commun.* **10**, 806 (2019).

33. A. Armin, R. D. Jansen-Van Vuuren, N. Kopidakis, P. L. Burn, P. Meredith, Narrowband light detection via internal quantum efficiency manipulation of organic photodiodes. *Nat. Commun.* **6**, 6343 (2015).

34. Q. Lin, A. Armin, P. L. Burn, P. Meredith, Filterless narrowband visible photodetectors. *Nat. Photonics* **9**, 687–694 (2015).

35. J. Wang, S. Xiao, W. Qian, K. Zhang, J. Yu, X. Xu, G. Wang, S. Zheng, S. Yang, Self-driven perovskite narrowband photodetectors with tunable spectral responses. *Adv. Mater.* **33**, 200555 (2021).

36. T. J. K. Brenner, Y. Vaynzof, Z. Li, D. Kabra, R. H. Friend, C. R. McNeill, White-light bias external quantum efficiency measurements of standard and inverted P3HT:PCBM photovoltaic cells. *J. Phys. D Appl. Phys.* **45**, 415101 (2012).

37. J. Liu, Y. Zou, B. Huang, Y. Gu, Y. Yang, Z. Han, Y. Zhang, X. Xu, H. Zeng, Sensitively switchable visible/infrared multispectral detection and imaging based on a tandem perovskite device. *Nanoscale* **12**, 20386–20395 (2020).

38. L. Li, Y. Deng, C. Bao, Y. Fang, H. Wei, S. Tang, F. Zhang, J. Huang, Self-filtered narrowband perovskite photodetectors with ultrafast and tuned spectral response. *Adv. Opt. Mater.* **5**, 1700672 (2017).

39. Y. Zhang, Z. Qin, X. Huo, D. Song, B. Qiao, S. Zhao, High-performance near-infrared photodetectors based on the synergy effect of short wavelength light filter and long wavelength response of a perovskite/polymer hybrid structure. *ACS Appl. Mater. Interfaces* **13**, 61818–61826 (2021).

40. B. Xie, R. Xie, K. Zhang, Q. Yin, Z. Hu, G. Yu, F. Huang, Y. Cao, Self-filtering narrowband high performance organic photodetectors enabled by manipulating localized Frenkel exciton dissociation. *Nat. Commun.* **11**, 2871 (2020).

41. B. Siegmund, A. Mischok, J. Benduhn, O. Zeika, S. Ullbrich, F. Nehm, M. Böhm, D. Spoltore, H. Fröb, C. Körner, K. Leo, K. Vandewal, Organic narrowband near-infrared photodetectors based on intermolecular charge-transfer absorption. *Nat. Commun.* **8**, 15421 (2017).

42. Z. Lan, L. Cai, D. Luo, F. Zhu, Narrowband near-infrared perovskite/polymer hybrid photodetectors. *ACS Appl. Mater. Interfaces* **13**, 981–988 (2021).

43. J. Zhao, X. Wang, Y. Xu, Y. Pan, Y. Li, J. Chen, Q. Li, X. Zhang, Z. Zhu, Z. Zhao, E. E. Elemike, D. C. Onwudiwe, B. S. Bae, S. Bin Shafie, W. Lei, Electrically modulated near-infrared/visible light dual-mode perovskite photodetectors. *ACS Appl. Mater. Interfaces* **13**, 25824–25833 (2022).

44. S. Qiao, Y. Liu, J. Liu, G. Fu, S. Wang, High-responsivity, fast, and self-powered narrowband perovskite heterojunction photodetectors with a tunable response range in the visible and near-infrared region. *ACS Appl. Mater. Interfaces* **13**, 34625–34636 (2021).

45. Y. S. Shin, Y. J. Yoon, J. Heo, S. Song, J. W. Kim, S. Y. Park, H. W. Cho, G. H. Kim, J. Y. Kim, Functionalized PFN-X (X = Cl, Br, or I) for balanced charge carriers of highly efficient blue light-emitting diodes. *ACS Appl. Mater. Interfaces* **12**, 35740–35747 (2020).

46. Q. Lin, A. Armin, D. M. Lyons, P. L. Burn, P. Meredith, Low noise, IR-blind organohalide perovskite photodiodes for visible light detection and imaging. *Adv. Mater.* **27**, 2060–2064 (2015).

47. Y. Wang, J. Kublitski, S. Xing, F. Dollinger, D. Spoltore, J. Benduhn, K. Leo, Narrowband organic photodetectors - towards miniaturized, spectroscopic sensing. *Mater. Horiz.* **9**, 220–251 (2022).

48. W. Zhang, C. Sun, I. Angunawela, L. Meng, S. Qin, L. Zhou, S. Li, H. Zhuo, G. Yang, Z. G. Zhang, H. Ade, Y. Li, 16.52% efficiency all-polymer solar cells with high tolerance of the photoactive layer thickness. *Adv. Mater.* **34**, 2108749 (2022).

49. B. H. Jiang, Y. P. Wang, C. Y. Liao, Y. M. Chang, Y. W. Su, R. J. Jeng, C. P. Chen, Improved blend film morphology and free carrier generation provide a high-performance ternary polymer solar cell. *ACS Appl. Mater. Interfaces* **13**, 1076–1085 (2021).

50. J. Yuan, Y. Zhang, L. Zhou, G. Zhang, H. L. Yip, T. K. Lau, X. Lu, C. Zhu, H. Peng, P. A. Johnson, M. Leclerc, J. Cao, J. Ulanski, Y. Li, Y. Zou, Single-junction organic solar cell with over 15% efficiency using fused-ring acceptor with electron-deficient core. *Joule* **3**, 1140–1151 (2019).

51. N. F. Watson, M. S. Badr, G. Belenky, D. L. Bliwise, O. M. Buxton, D. Buysse, D. F. Dinges, J. Gangwisch, M. A. Grandner, C. Kushida, R. K. Malhotra, J. L. Martin, S. R. Patel, S. F. Quan, E. Tasali, M. Twery, J. B. Croft, E. Maher, J. A. Barrett, S. M. Thomas, J. L. Heald, Joint consensus statement of the American Academy of Sleep Medicine and Sleep Research Society on the recommended amount of sleep for a healthy adult: Methodology and discussion. *J. Clin. Sleep Med.* **11**, 931–952 (2015).

52. S. Xing, J. Kublitski, C. Hänisch, L. C. Winkler, T.-y. Li, H. Kleemann, J. Benduhn, K. Leo, Photomultiplication-type organic photodetectors for near-infrared sensing with high and bias-independent specific detectivity. *Adv. Sci.* **9**, 2105113 (2022).

53. Y. Wang, Y. Liu, S. Cao, J. Wang, A review on solution-processed perovskite/organic hybrid photodetectors. *J. Mater. Chem. C.* **9**, 5302–5322 (2021).

54. Z. Lan, M.-H. Lee, F. Zhu, Recent advances in solution-processable organic photodetectors and applications in flexible electronics. *Adv. Intell. Syst.* **4**, 2100167 (2022).

55. E. Allado, M. Poussel, J. Renno, A. Moussu, O. Hily, M. Temperelli, E. Albuisson, B. Chenuel, Remote photoplethysmography is an accurate method to remotely measure respiratory rate: A hospital-based trial. *J. Clin. Med.* **11**, 3647 (2022).

56. J. Wang, K. Datta, J. Li, M. A. Verheijen, D. Zhang, M. M. Wienk, R. A. J. Janssen, Understanding the film formation kinetics of sequential deposited narrow-bandgap Pb–Sn hybrid perovskite films. *Adv. Energy Mater.* **10**, 2000566 (2020).

57. M. Mulato, C. M. Hong, S. Wagner, Size and etching effects on the reverse current of a-Si:H p-i-n diodes. *J. Electrochem. Soc.* **150**, G735 (2003).

58. A. J. J. M. van Breemen, R. Ollearo, S. Shanmugam, B. Peeters, L. C. J. M. Peters, R. L. van de Ketterij, I. Katsouras, H. B. Akkerman, C. H. Frijters, F. Di Giacomo, S. Veenstra, R. Andriessen, R. A. J. Janssen, E. A. Meulenkamp, G. H. Gelinck, A thin and flexible scanner for fingerprints and documents based on metal halide perovskites. *Nat. Electron* **4**, 818–826 (2021).

59. Q. Liu, S. Zeiske, X. Jiang, D. Desta, S. Mertens, S. Gielen, R. Shanivarasanthe, H. G. Boyen, A. Armin, K. Vandewal, Electron-donating amine-interlayer induced n-type doping of polymer: Nonfullerene blends for efficient narrowband near-infrared photo-detection. *Nat. Commun.* **13**, 5194 (2022).

60. C. Kaiser, K. S. Schellhammer, J. Benduhn, B. Siegmund, M. Tropiano, J. Kublitski, D. Spoltore, M. Panhans, O. Zeika, F. Ortmann, P. Meredith, A. Armin, K. Vandewal, Manipulating the charge transfer absorption for narrowband light detection in the near-infrared. *Chem. Mater.* **31**, 9325–9330 (2019).

61. L. Shen, Y. Zhang, Y. Bai, X. Zheng, Q. Wang, J. Huang, A filterless, visible-blind, narrowband, and near-infrared photodetector with a gain. *Nanoscale* **8**, 12990–12997 (2016).

62. M. Liu, J. Wang, Z. Zhao, K. Yang, P. Durand, F. Ceugniet, G. Ulrich, L. Niu, Y. Ma, N. Leclerc, X. Ma, L. Shen, F. Zhang, Ultra-narrow-band NIR photomultiplication organic photodetectors based on charge injection narrowing. *J. Phys. Chem. Lett.* **12**, 2937–2943 (2021).

63. W. Wang, M. Du, M. Zhang, J. Miao, Y. Fang, F. Zhang, Organic photodetectors with gain and broadband/narrowband response under top/bottom illumination conditions. *Adv. Opt. Mater.* **6**, 1800249 (2018).

64. W. Cheng, W. Tian, F. Cao, L. Li, Self-powered bifunctional perovskite photodetectors with both broadband and narrowband photoresponse. *InfoMat* **4**, e12348 (2022).

65. J. Miao, F. Zhang, M. Du, W. Wang, Y. Fang, Photomultiplication type organic photodetectors with broadband and narrowband response ability. *Adv. Opt. Mater.* **6**, 1800001 (2018).